Electronic Supplementary Information

Enhancement in the Thermoelectric Performance of Colusites $Cu_{26}A_2E_6S_{32}$ (A = Nb, Ta; E = Sn, Ge) using E-site Non-stoichiometry

Yohan Bouyrie[a], Michihiro Ohta[a*], Koichiro Suekuni[b], Yuta Kikuchi[a], Priyanka Jood[a], Atsushi Yamamoto[a], Toshiro Takabatake[c]

[a] *Research Institute for Energy Conservation, National Institute of Advanced Industrial Science and Technology (AIST), Tsukuba, Ibaraki 305-8568, Japan*

[b] *Department of Applied Science for Electronics and Materials, Interdisciplinary Graduate School of Engineering Sciences, Kyushu University, Kasuga, Fukuoka 816-8580, Japan*

[c] *Department of Quantum Matter, ADSM, Hiroshima University, Higashi-Hiroshima, Hiroshima 739-8530, Japan*

*Corresponding Author: Michihiro Ohta

Email: ohta.michihiro@aist.go.jp

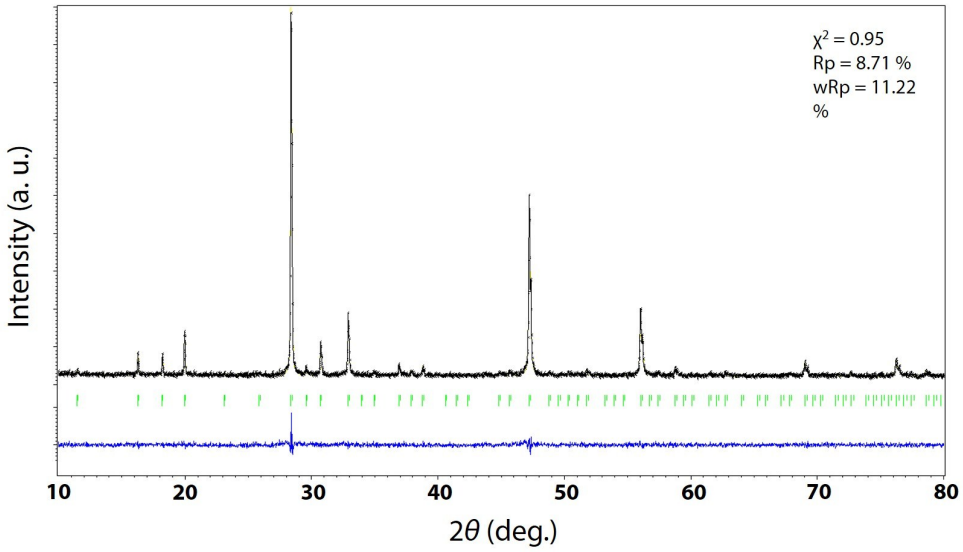

Figure S1

Le Bail refinement of the powder X-ray diffraction pattern of the sintered compact of $Cu_{26}Nb_2Sn_{5.5}S_{32}$. The experimental data are marked as red dots, the calculated pattern is in black and the difference between experimental and calculated patterns is shown in blue. The vertical green bars stand for the expected Bragg positions of the cubic crystal lattice of colusites.

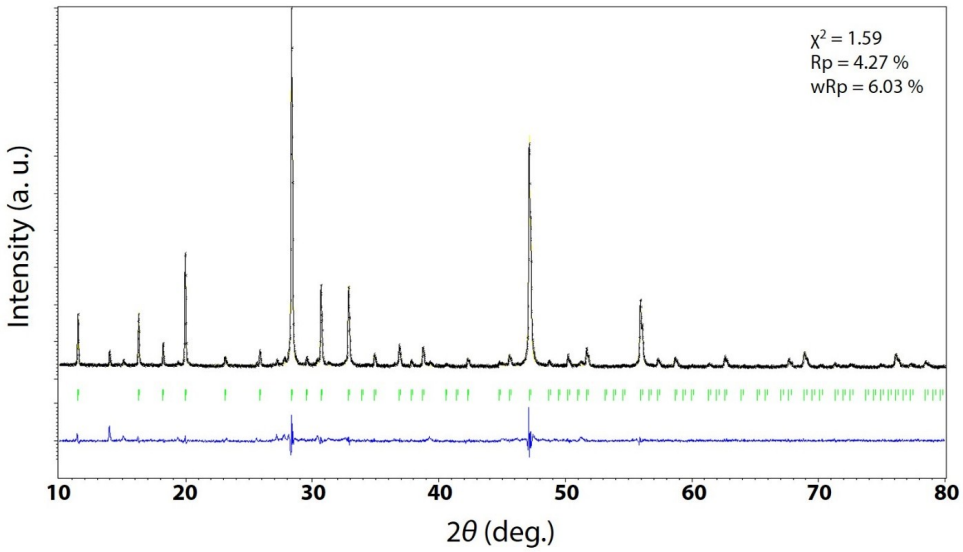

Figure S2

Le Bail refinement of the powder X-ray diffraction pattern of the sintered compact of $Cu_{26}Ta_2Sn_{5.5}S_{32}$. The experimental data are marked as red dots, the calculated pattern is in black and the difference between experimental and calculated patterns is shown in blue. The vertical green bars stand for the expected Bragg positions of the cubic crystal lattice of colusites.

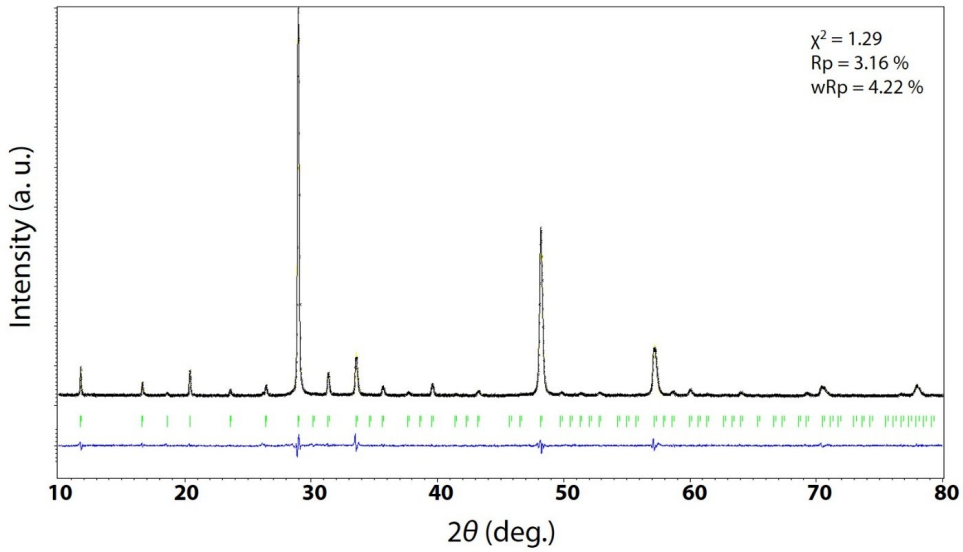

Figure S3

Le Bail refinement of the powder X-ray diffraction pattern of the sintered compact of $Cu_{26}Nb_2Ge_{6.0}S_{32}$. The experimental data are marked as red dots, the calculated pattern is in black and the difference between experimental and calculated patterns is shown in blue. The vertical green bars stand for the expected Bragg positions of the cubic crystal lattice of colusites.

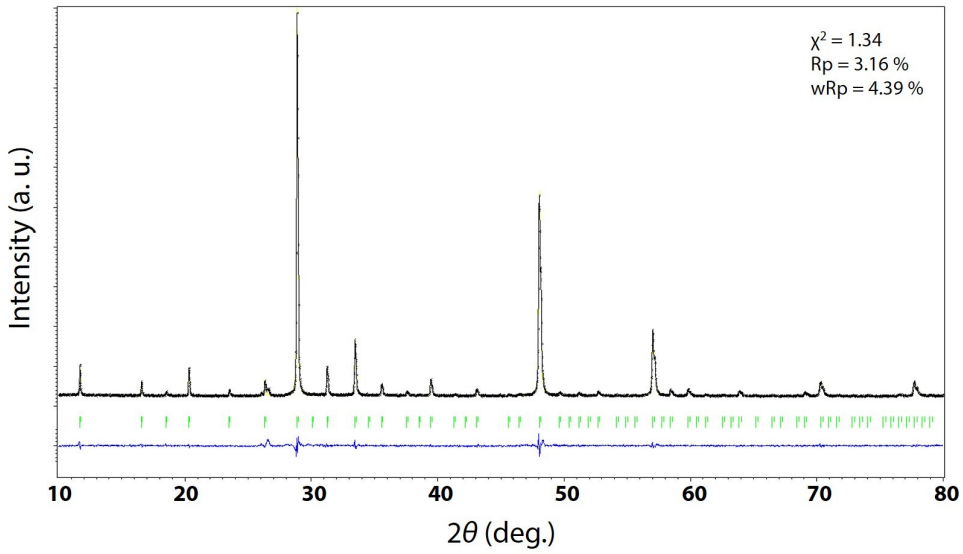

Figure S4

Le Bail refinement of the powder X-ray diffraction pattern of the sintered compact of $Cu_{26}Nb_2Ge_{5.5}S_{32}$. The experimental data are marked as red dots, the calculated pattern is in black and the difference between experimental and calculated patterns is shown in blue. The vertical green bars stand for the expected Bragg positions of the cubic crystal lattice of colusites.

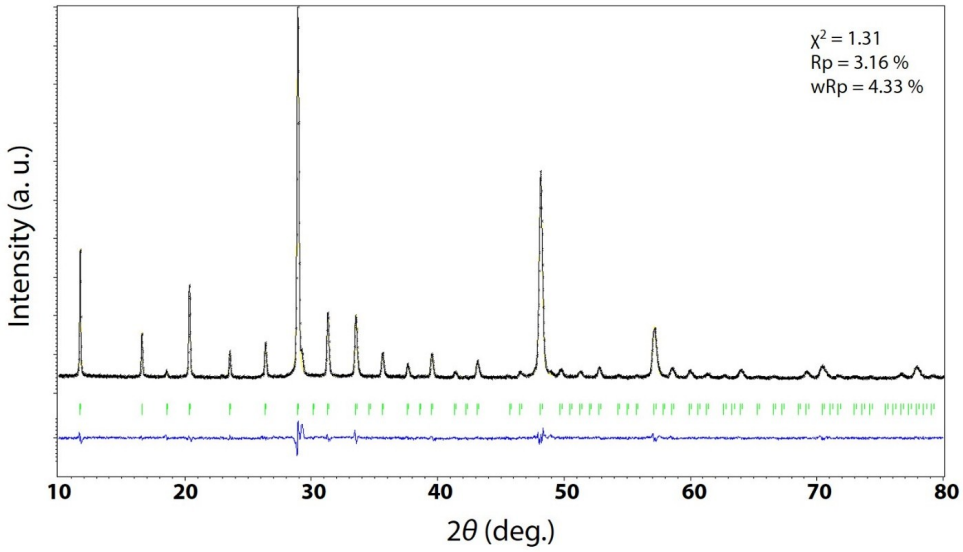

Figure S5

Le Bail refinement of the powder X-ray diffraction pattern of the sintered compact of $Cu_{26}Ta_2Ge_{6.0}S_{32}$. The experimental data are marked as red dots, the calculated pattern is in black and the difference between experimental and calculated patterns is shown in blue. The vertical green bars stand for the expected Bragg positions of the cubic crystal lattice of colusites.

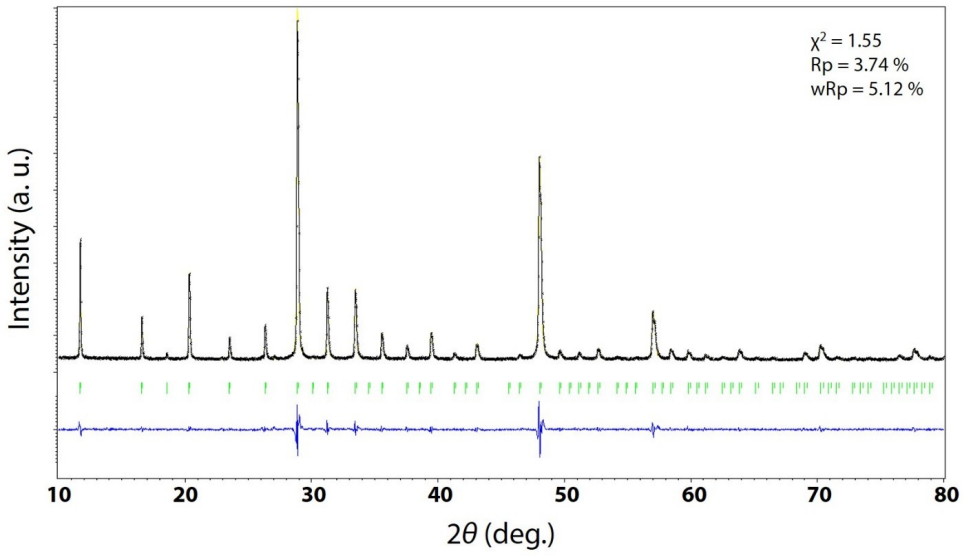

Figure S6

Le Bail refinement of the powder X-ray diffraction pattern of the sintered compact of $Cu_{26}Ta_2Ge_{5.5}S_{32}$. The experimental data are marked as red dots, the calculated pattern is in black and the difference between experimental and calculated patterns is shown in blue. The vertical green bars stand for the expected Bragg positions of the cubic crystal lattice of colusites.

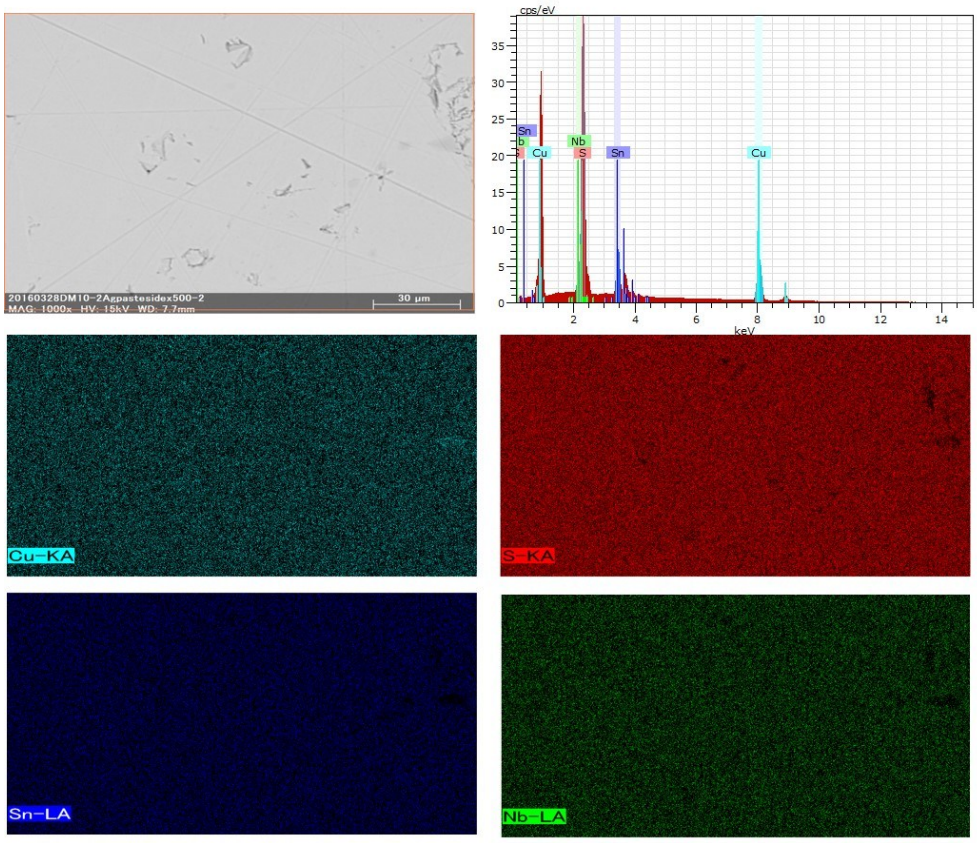

Figure S7

Scanning electron microscopy-backscattered electron microscopy image and corresponding X-ray maps of the sintered compact of $Cu_{26}Nb_2Sn_{5.5}S_{32}$ showing the good chemical homogeneity of the sample.

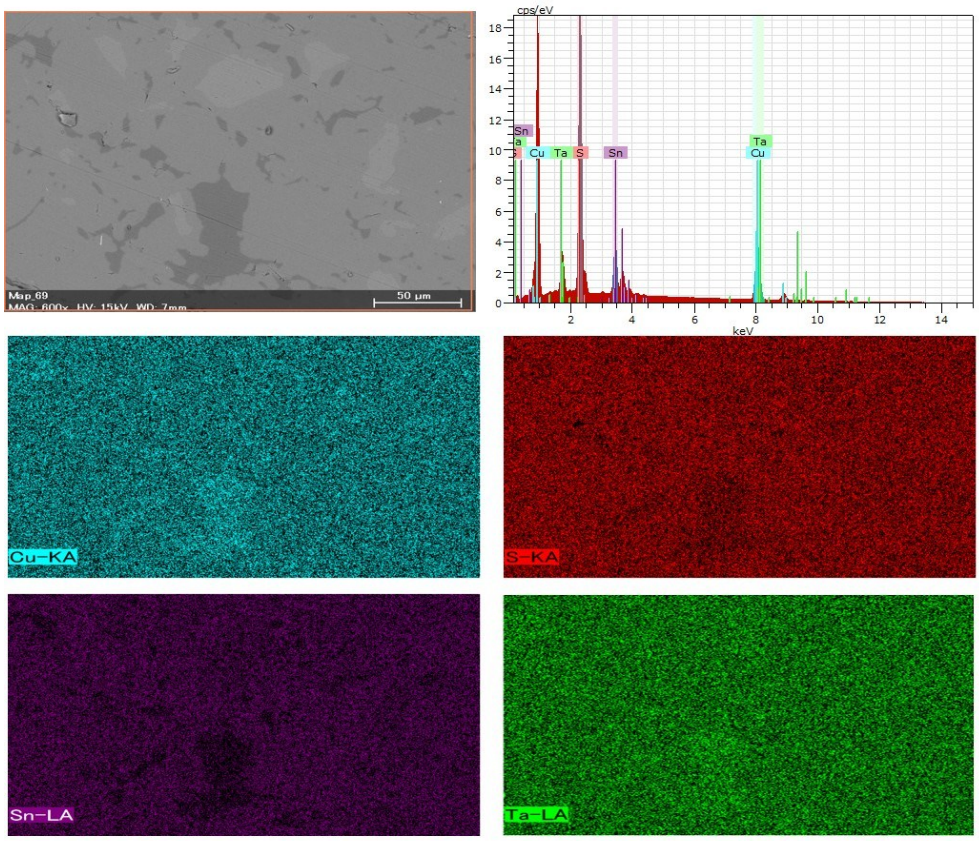

Figure S8

Scanning electron microscopy-backscattered electron microscopy image and corresponding X-ray maps of the sintered compact of $Cu_{26}Ta_2Sn_{5.5}S_{32}$ showing the good chemical homogeneity of the sample with presence of microscale precipitates.

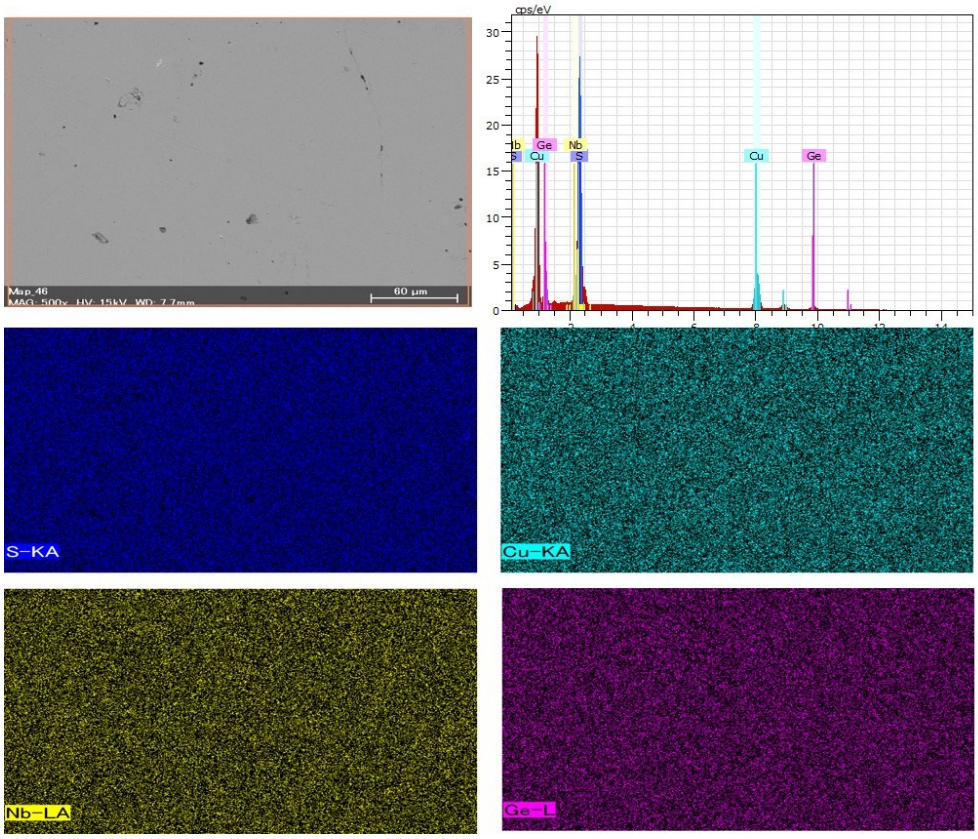

Figure S9

Scanning electron microscopy-backscattered electron microscopy image and corresponding X-ray maps of the sintered compact of $Cu_{26}Nb_2Ge_{6.0}S_{32,}$ showing the good chemical homogeneity of the sample.

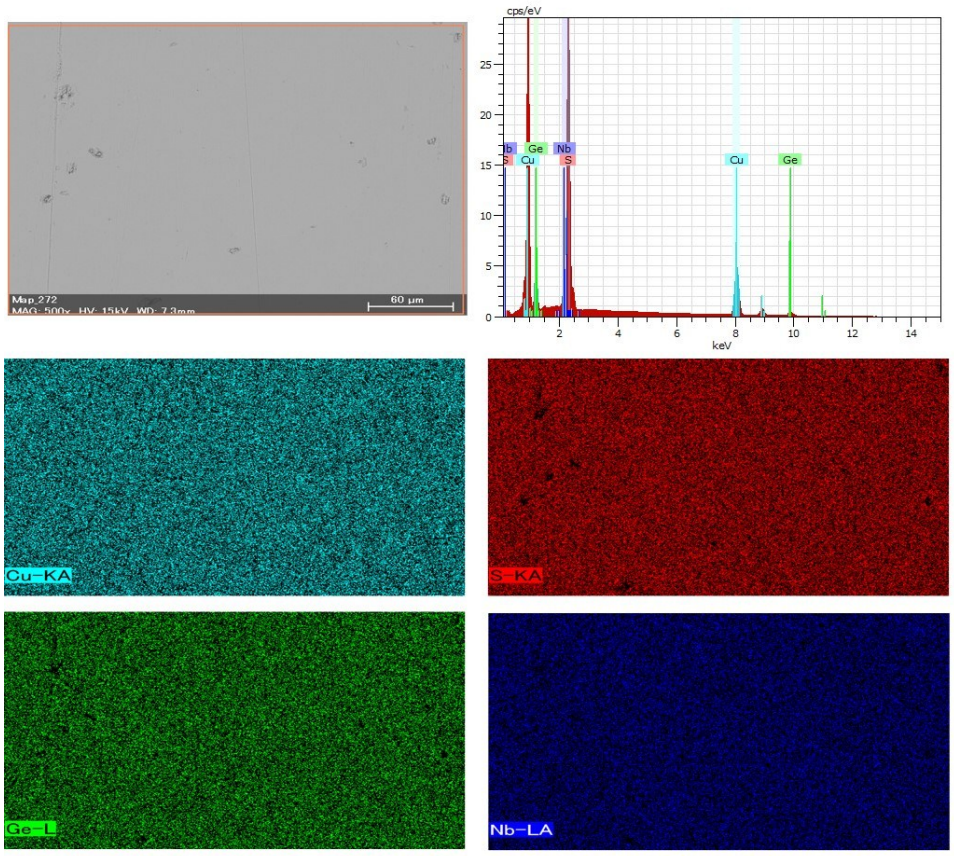

Figure S10

Scanning electron microscopy-backscattered electron microscopy image and corresponding X-ray maps of the sintered compact of $Cu_{26}Nb_2Ge_{5.5}S_{32}$ showing the good chemical homogeneity of the sample.

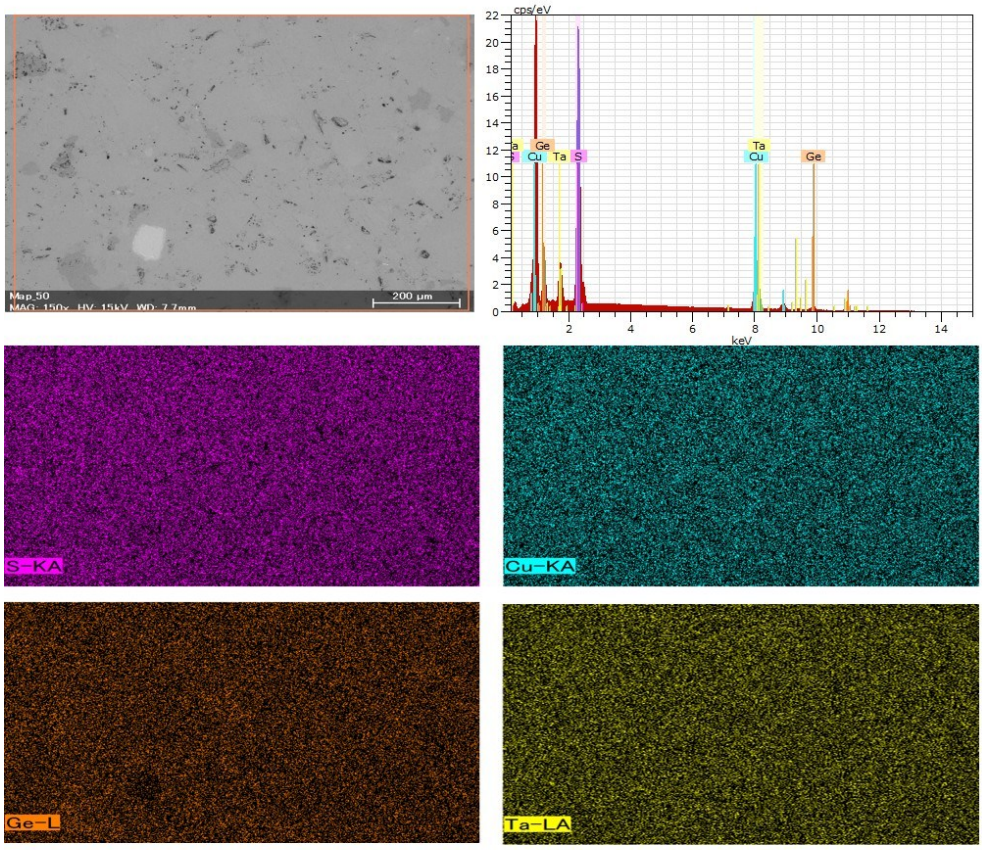

Figure S11

Scanning electron microscopy-backscattered electron microscopy image and corresponding X-ray maps of the sintered compact of $Cu_{26}Ta_2Ge_{6.0}S_{32}$ showing the good chemical homogeneity of the sample with presence of microscale precipitates.

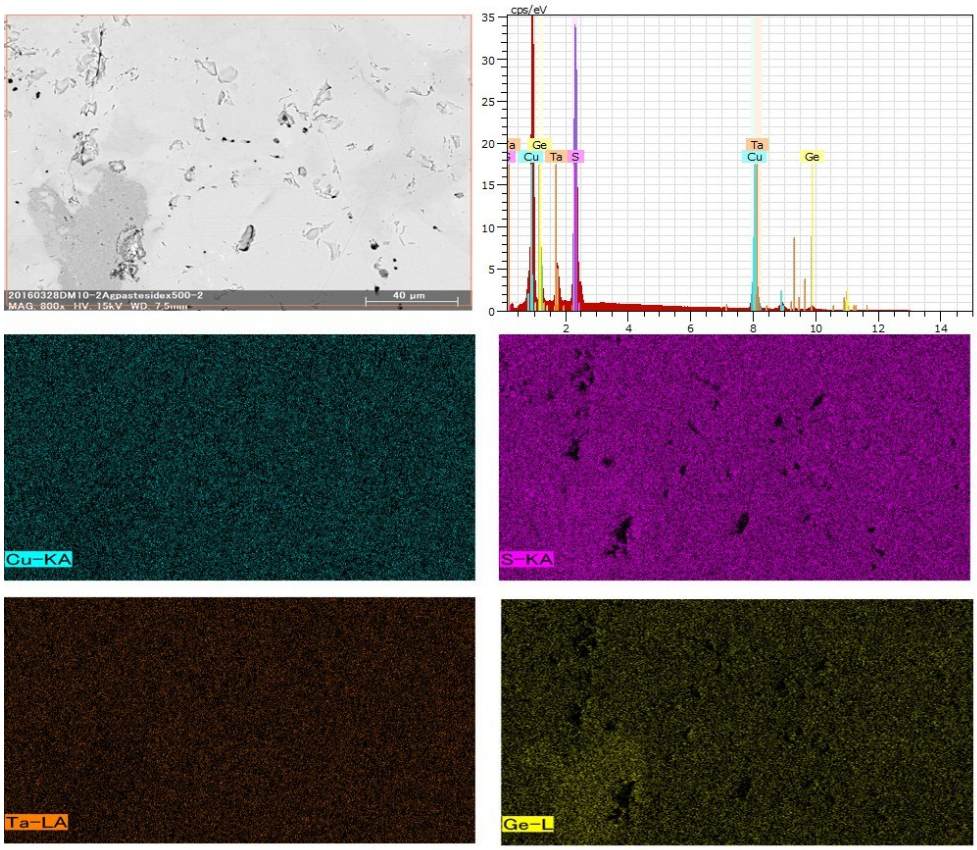

Figure S12

Scanning electron microscopy-backscattered electron microscopy image and corresponding X-ray maps of the sintered compact of $Cu_{26}Ta_2Ge_{5.5}S_{32}$ showing the good chemical homogeneity of the sample with presence of microscale precipitates.

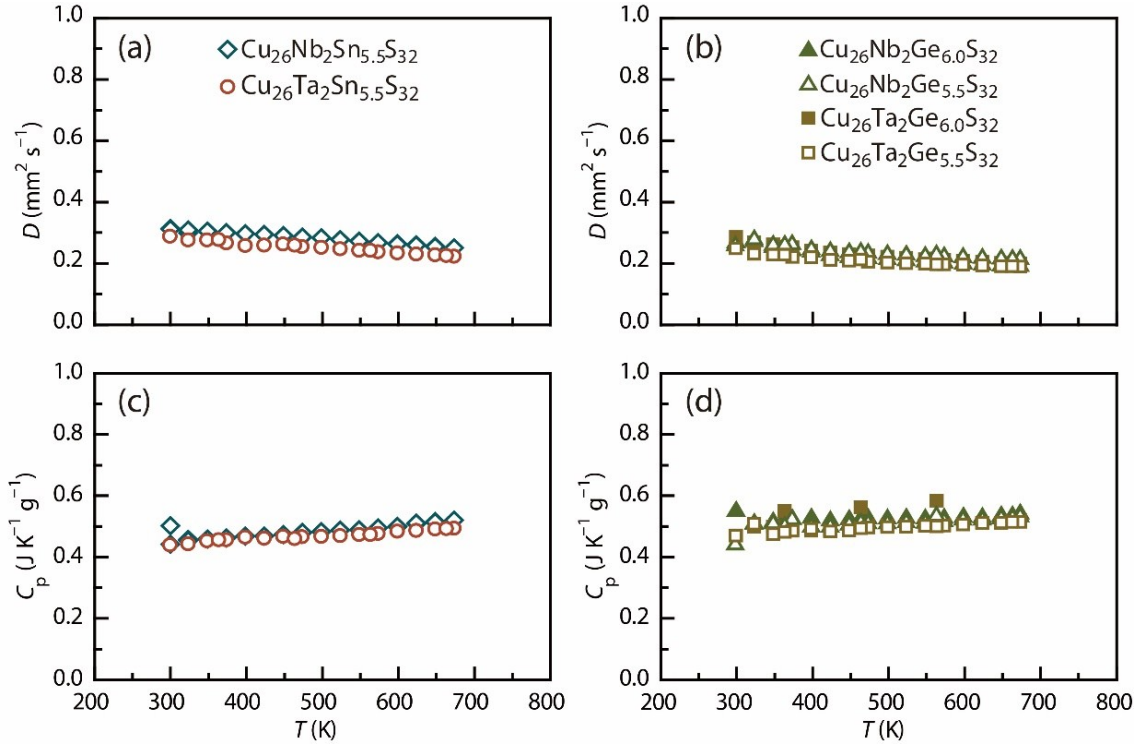

Figure S13

Temperature dependence of the (a,b) thermal diffusivity D and (c,d) Specific heat C_p for the sintered compacts of $Cu_{26}A_2Sn_{5.5}S_{32}$ (A = Nb, Ta) and $Cu_{26}A_2Ge_{6-x}S_{32}$ (A = Nb, Ta; x = 0, 0.5).

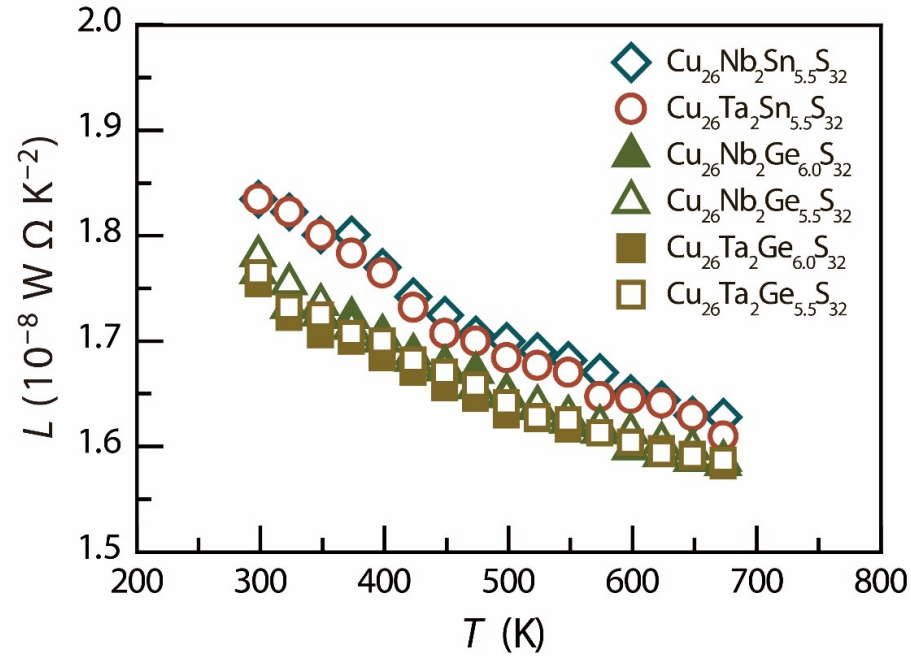

Figure S14

Temperature dependence of the estimated Lorentz number L for the sintered compacts of $Cu_{26}A_2Sn_{5.5}S_{32}$ (A = Nb, Ta) and $Cu_{26}A_2Ge_{6-x}S_{32}$ (A = Nb, Ta; x = 0, 0.5).

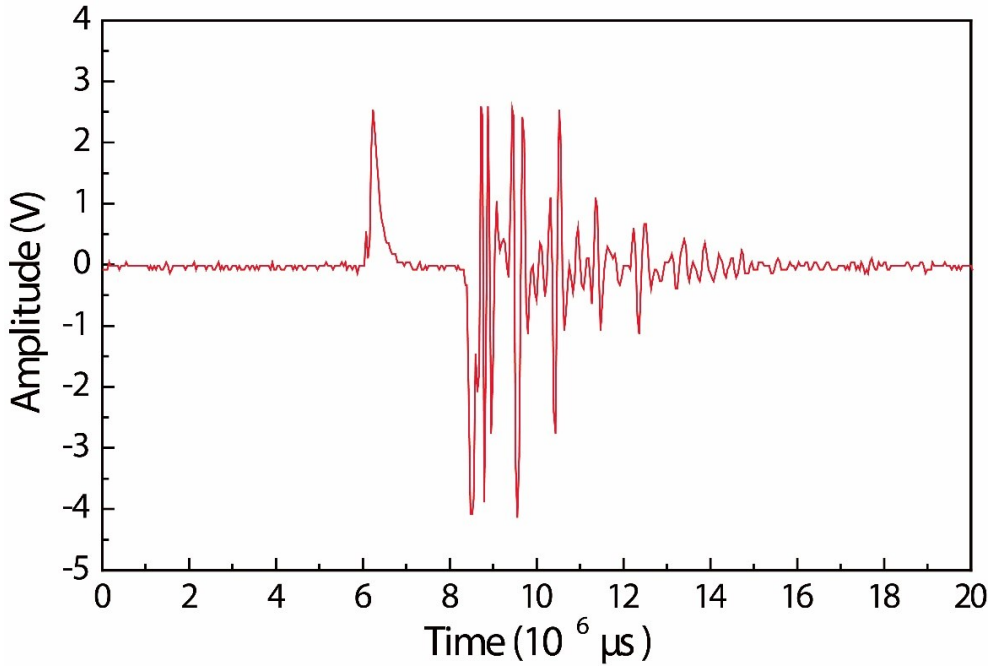

Figure S15

Pulse-echo pattern of the sintered compact of $Cu_{26}Nb_2Sn_{6.0}S_{32}$ using longitudinal contact transducer (5MHz).

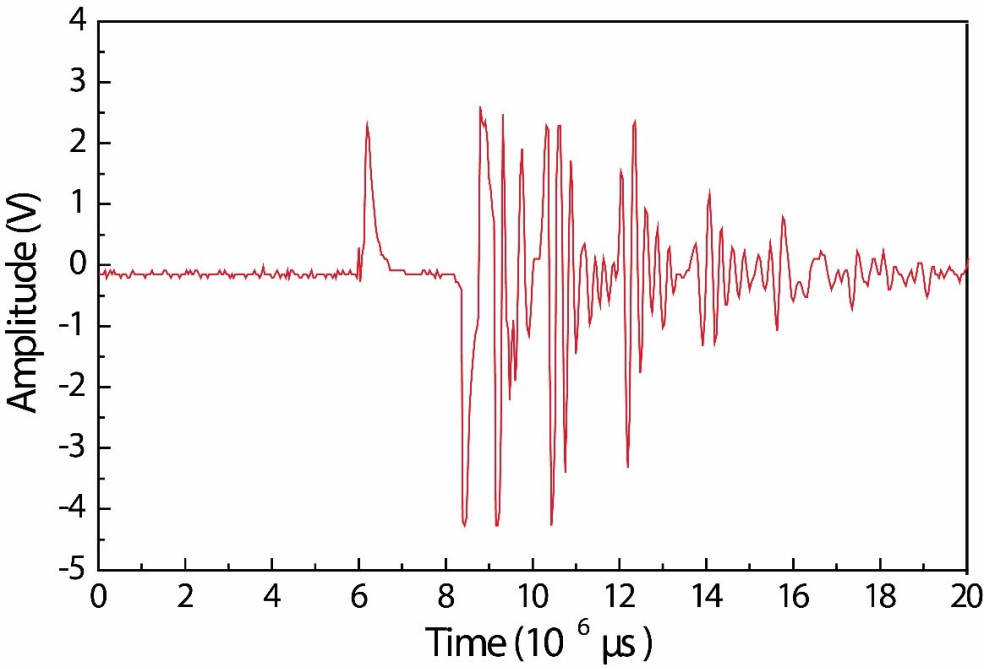

Figure S16

Pulse-echo pattern of the sintered compact of $Cu_{26}Nb_2Sn_{6.0}S_{32}$ using transverse contact transducer (5MHz).

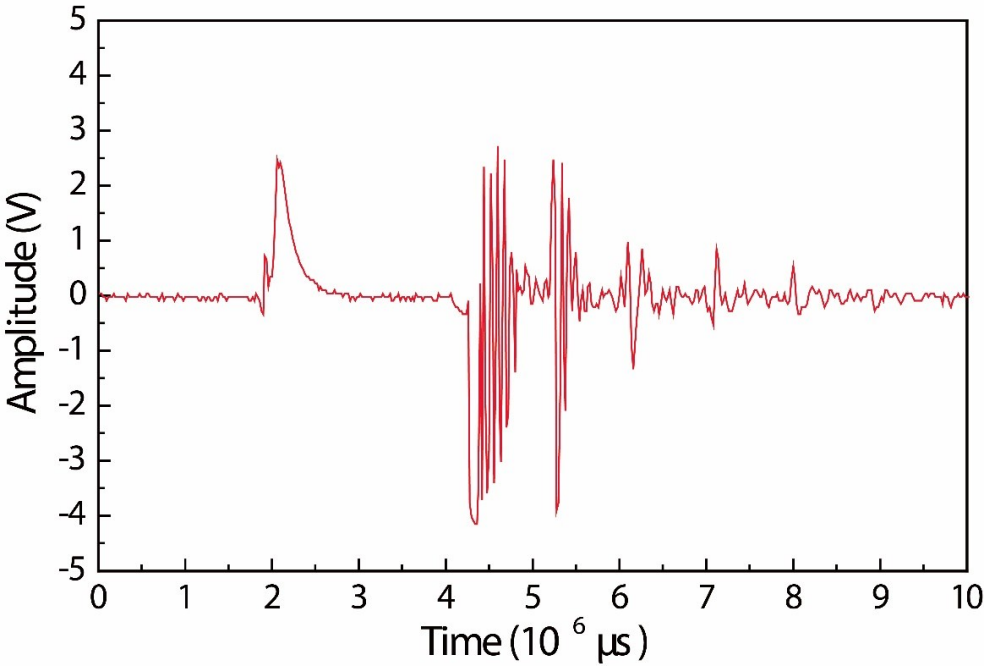

Figure S17

Pulse-echo pattern of the sintered compact of $Cu_{26}Nb_2Sn_{6.0}S_{32}$ using longitudinal contact transducer (15MHz).

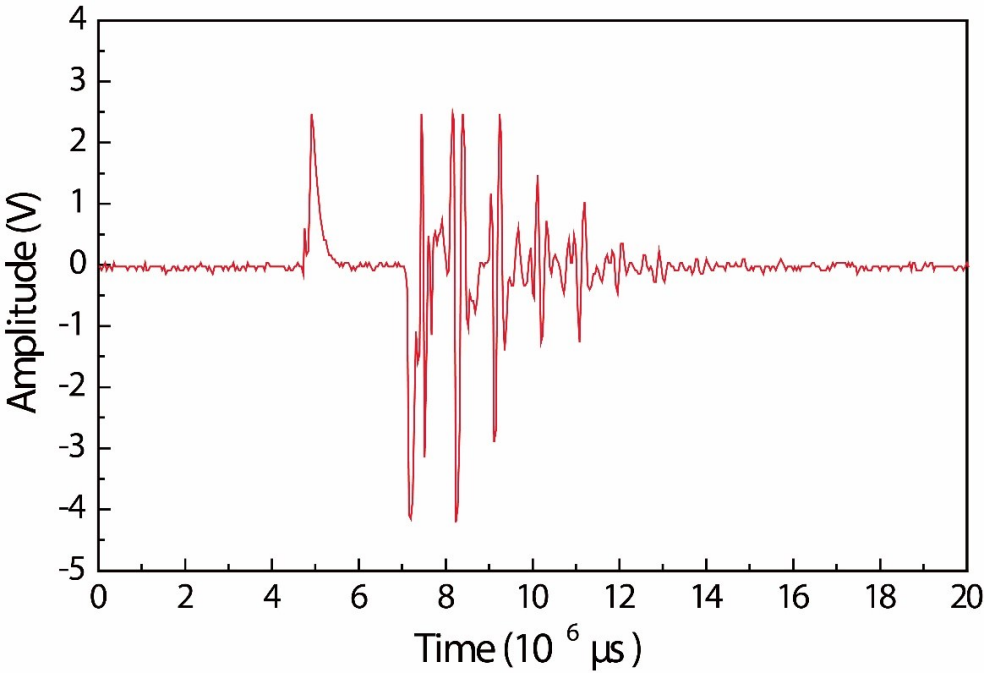

Figure S18

Pulse-echo pattern of the sintered compact of $Cu_{26}Nb_2Sn_{5.5}S_{32}$ using longitudinal contact transducer (5MHz).

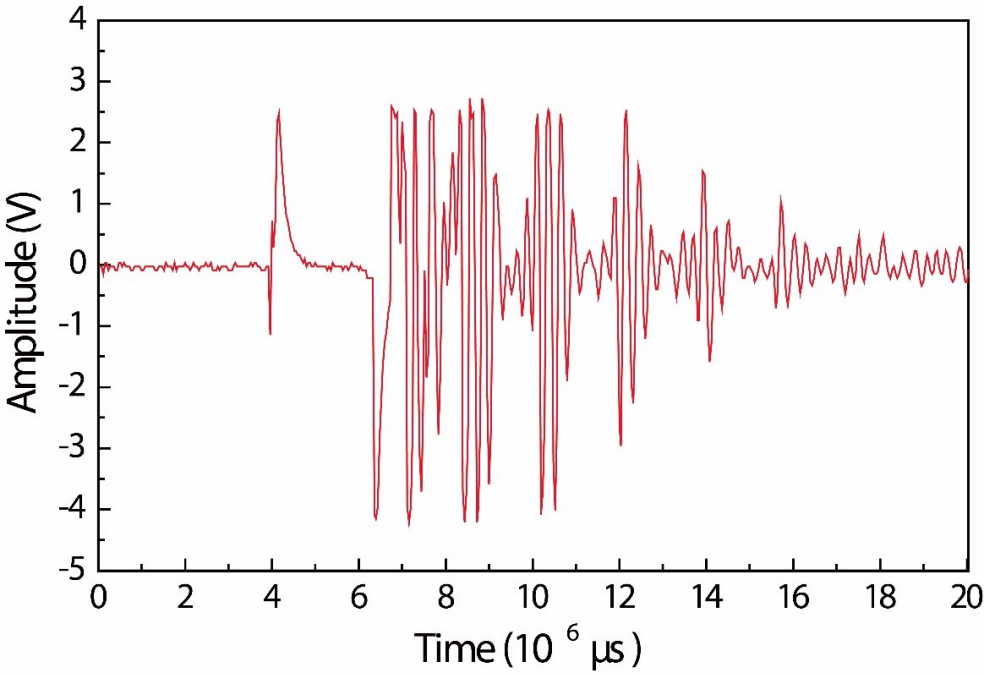

Figure S19

Pulse-echo pattern of the sintered compact of $Cu_{26}Nb_2Sn_{5.5}S_{32}$ using transverse contact transducer (5MHz).

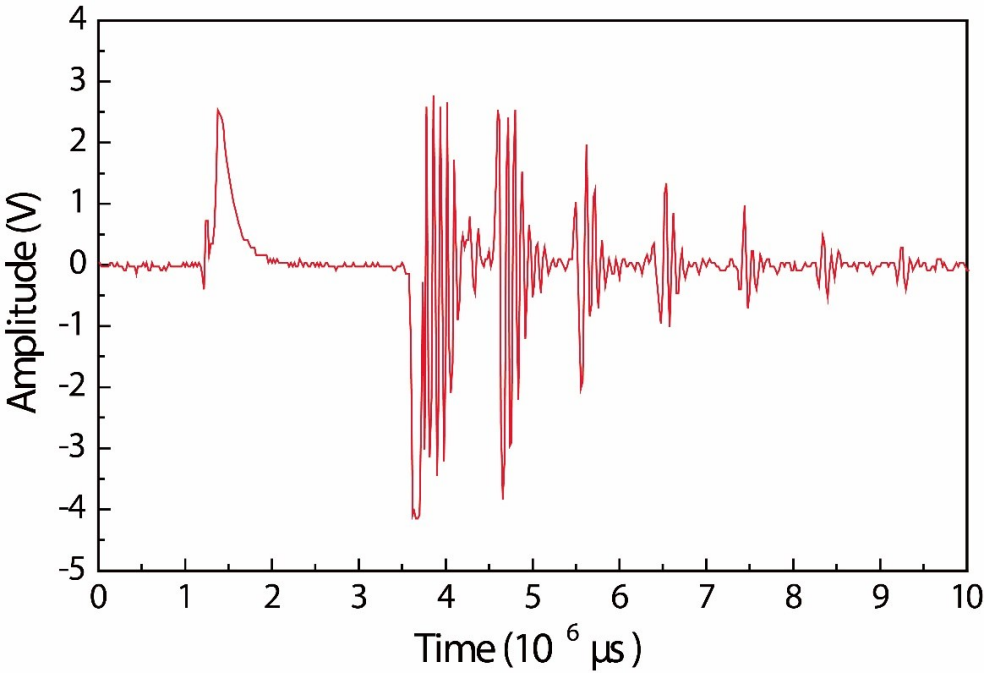

Figure S20

Pulse-echo pattern of the sintered compact of $Cu_{26}Nb_2Sn_{5.5}S_{32}$ using longitudinal contact transducer (15MHz).

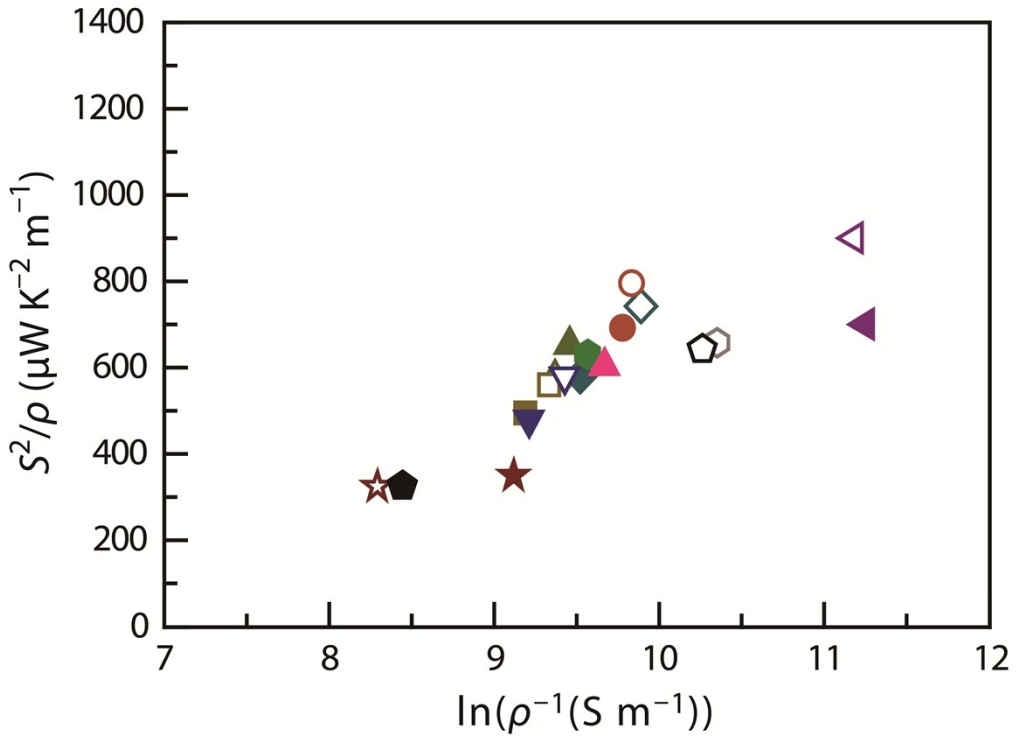

Figure S21

The power factor S^2/ρ versus logarithm of the inverse of the electrical resistivity ln ρ^{-1} at 670 K for the E = Sn samples $Cu_{26}A_2Sn_{5.5}S_{32}$ (A = Nb, Ta) and E = Ge samples $Cu_{26}A_2Ge_{6-x}S_{32}$ (A = Nb, Ta; x = 0, 0.5): $Cu_{26}Nb_2Sn_{5.5}S_{32}$ (cyan open diamond), $Cu_{26}Ta_2Sn_{5.5}S_{32}$ (red open circle), $Cu_{26}Nb_2Ge_{6.0}S_{32}$ (dark-green filled triangle), $Cu_{26}Nb_2Ge_{5.5}S_{32}$ (dark-green open triangle), $Cu_{26}Ta_2Ge_{6.0}S_{32}$ (dark-yellow filled square), and $Cu_{26}Ta_2Ge_{5.5}S_{32}$ (dark-yellow open square). Data for colusites in the literature are also included for comparison: $Cu_{26}V_2Ge_6S_{32}$ (green filled hexagon, 663 K)[50], $Cu_{26}V_2Sn_6S_{32}$ (blue filled inversed triangle, 663 K)[50], $Cu_{26}V_2Sn_6S_{32}$ (pink filled triangle, 660 K)[55], $Cu_{26}Nb_2Sn_6S_{32}$ (cyan filled diamond, 660 K)[55], $Cu_{26}Ta_2Sn_6S_{32}$ (red filled circle, 660 K)[55], $Cu_{26}V_2Sn_{5.5}S_{32}$ (blue inversed open triangle, 660 K)[56], $Cu_{25}Zn_1V_2Sn_6S_{32}$ (brown filled star, 660 K)[56], $Cu_{24}Zn_2V_2Sn_6S_{32}$ (brown open star, 660 K)[56], $Cu_{24}Co_2V_2Ge_6S_{32}$ (black filled pentagon, 665 K)[57], $Cu_{24}Ni_2V_2Ge_6S_{32}$ (black open pentagon, 665 K)[57], $Cu_{26}V_2Sn_6S_{32}$ (purple tilted filled triangle, 675 K)[58], $Cu_{25}Zn_1V_2Sn_6S_{32}$ (purple tilted open triangle, 675 K)[58], and $Cu_{24}Zn_2V_2Sn_6S_{32}$ (gray open hexagon, 675 K)[58].

Table S1

Measured density d_{meas}, and theoretical density d_{theo} of the sintered compacts of $Cu_{26}A_2Sn_{5.5}S_{32}$ (A = Nb, Ta) and $Cu_{26}A_2Ge_{6-x}S_{32}$ (A = Nb, Ta; x = 0, 0.5).

	d_{meas} (g cm^{-3})	d_{theo} (g cm^{-3})
	300 K	300 K
$Cu_{26}Nb_2Sn_{5.5}S_{32}$	4.80	4.54
$Cu_{26}Ta_2Sn_{5.5}S_{32}$	5.03	4.74
$Cu_{26}Nb_2Ge_{6.0}S_{32}$	4.57	4.49
$Cu_{26}Nb_2Ge_{5.5}S_{32}$	4.67	4.57
$Cu_{26}Ta_2Ge_{6.0}S_{32}$	4.84	4.73
$Cu_{26}Ta_2Ge_{5.5}S_{32}$	4.90	4.65

Table S2

Chemical compositions of the colusite matrix of the sintered compacts of the E = Sn samples $Cu_{26}A_2Sn_{5.5}S_{32}$ (A = Nb, Ta), determined by energy dispersive X-ray spectroscopy analysis. The compositions were calculated using two assumptions: (i) the sum of the number of cations (Cu, A, and Sn) is 34, and (ii) the number of S atoms in the unit cell is 32. The standard deviation of the mean composition is given in parentheses. Data for the stoichiometric samples $Cu_{26}A_2Sn_{6.0}S_{32}$ are also listed for comparison[55].

Sample	Chemical composition				
$Cu_{26}Nb_2Sn_{6.0}S_{32}$		Cu	Nb	Sn	S
	Nominal	26	2	6.0	32
	(i) Cation content: 34	27.0(19)	1.9(2)	5.1(6)	28.6(18)
	(ii) Sulfur content: 32	30.2(13)	2.2(1)	5.7(6)	32
$Cu_{26}Nb_2Sn_{5.5}S_{32}$		Cu	Nb	Sn	S
	Nominal	26	2	5.5	32
	(i) Cation content: 34	27.0(12)	2.0(1)	5.0(5)	28.7(13)
	(ii) Sulfur content: 32	30.2(11)	2.3(1)	5.6(6)	32
$Cu_{26}Ta_2Sn_{6.0}S_{32}$		Cu	Ta	Sn	S
	Nominal	26	2	6.0	32
	(i) Cation content: 34	26.3(14)	2.3(4)	5.4(4)	29.2(15)
	(ii) Sulfur content: 32	28.8(13)	2.6(5)	5.9(4)	32
$Cu_{26}Ta_2Sn_{5.5}S_{32}$		Cu	Ta	Sn	S
	Nominal	26	2	5.5	32
	(i) Cation content: 34	26.8(25)	2.1(4)	5.1(6)	29.1(28)
	(ii) Sulfur content: 32	29.5(19)	2.4(4)	5.6(5)	32

Table S3

Chemical compositions of the colusite matrix of the sintered compacts of the E = Ge samples $Cu_{26}A_2Ge_{6-x}S_{32}$ (A = Nb, Ta; x = 0, 0.5) determined by energy dispersive X-ray spectroscopy analysis. The compositions were calculated using two assumptions: (i) the sum of the number of cations (Cu, A, and Ge) is 34, and (ii) the number of S atoms in the unit cell is 32. The standard deviation of the mean composition is given in parentheses.

Sample	Chemical composition				
$Cu_{26}Nb_2Ge_{6.0}S_{32}$		Cu	Nb	Ge	S
	Nominal	26	2	6.0	32
	(i) Cation content: 34	26.4(15)	1.8(2)	5.8(4)	28.1(16)
	(ii) Sulfur content: 32	30.1 (15)	2.0(2)	6.6(4)	32
$Cu_{26}Nb_2Ge_{5.5}S_{32}$		Cu	Nb	Ge	S
	Nominal	26	2	5.5	32
	(i) Cation content: 34	24.6(14)	1.6(2)	5.9(4)	28.1(15)
	(ii) Sulfur content: 32	30.1(14)	1.9(2)	6.7(4)	32
$Cu_{26}Ta_2Ge_{6.0}S_{32}$		Cu	Ta	Ge	S
	Nominal	26	2	6.0	32
	(i) Cation content: 34	25.9(26)	2.5(8)	5.5(8)	28.6(27)
	(ii) Sulfur content: 32	29.3(13)	2.8(8)	6.2(7)	32
$Cu_{26}Ta_2Ge_{5.5}S_{32}$		Cu	Ta	Ge	S
	Nominal	26	2	5.5	32
	(i) Cation content: 34	26.4(19)	2.0(6)	5.7(6)	28.6(21)
	(ii) Sulfur content: 32	29.5(15)	2.2(6)	6.3(6)	32